MIT Open Access Articles

Flow patterns around two neighboring patches of emergent vegetation and possible implications for deposition and vegetation growth

Massachusetts Institute of Technology

Flow patterns around two neighboring patches of emergent vegetation and possible implications for deposition and vegetation growth.

Paulo H. S. de Lima[1*], Johannes G. Janzen[1], Heidi M. Nepf[2].

1

Faculty of Engineering, Architecture and Urban Planning, and Geography

Federal University of Mato Grosso do Sul

Campo Grande, Mato Grosso do Sul, Brazil, paulo.lima@ufms.br

*Corresponding Author

2

Department of Civil and Environmental Engineering

Massachusetts Institute of Technology

Cambridge, Massachusetts, USA.

Abstract

The flow around two neighboring, circular, vegetation patches of equal diameter (D) was investigated using Computational Fluid Dynamics (CFD). Depending on the patches' transverse and longitudinal center-to-center spacing (T and L, respectively), several distinct flow patterns were observed. The patterns are compared to flow near an isolated patch. The key flow patterns were interpreted in terms of implications for deposition. Deposition maps were calculated for two different threshold velocities: $0.5U_0$ and $0.7U_0$, where U_0 is the free stream velocity. When the two patches were far away from each other, the interaction of their wakes was weak, and the flow and deposition pattern around each patch resembled that of a single, isolated patch. When the patches were very close, wake interaction took place, resulting in additional deposition along the centerline between the two patches, but further downstream than the deposition in line with each patch. For some intermediate patch spacings, the wake of the upstream patch was dramatically shortened, relative to an isolated patch, and the wake of the downstream patch was lengthened. The results show that flow distribution is influenced by interaction between neighboring vegetation patches and suggest that this may create feedbacks that influence the evolution of vegetated landscapes.

1. Introduction

Vegetated landscapes provide a variety of ecosystem services, including providing habitat [1], producing oxygen [2], reducing turbidity [3], and decreasing bank erosion [4]. These landscapes develop over time scales of decades to millennia through the action of vegetation-flow-sediment feedbacks: the presence of vegetation modifies the spatial distribution of water flow, and thus sedimentation and erosion. Subsequently, changes to water flow, sedimentation, and erosion patterns affect the spatial pattern of vegetation establishment [5-7]. Understanding these vegetation-flow-sediment feedbacks is important to predict the outcomes of river management actions [8-10].

Recent research has improved the understanding of vegetation-flow-sediment feedbacks created by isolated, finite vegetation patches. Velocity declines 1 to 2 patch diameters (D) upstream of the patch, as flow is diverted around the region of high drag caused by the presence of the vegetation [7, 11, 12]. The diversion of flow around the patch produces locally enhanced flow along the vegetation edge, which promotes erosion and may inhibit the lateral expansion of the patch, a negative feedback [8, 9, 13, 14]. Because the patches are porous, some flow penetrates through the patches into the wake, sometimes referred to as bleed flow. The bleed flow entering the wake delays the onset of the von Kármán vortex street until a distance L_1 behind the patch. Over the distance L_1 behind the patch, which we call the near wake region, the mean and turbulent velocity are depressed, relative to the free stream, and this encourages the deposition of fine sediment, creating conditions that favor new vegetation growth and thus patch expansion in the streamwise direction, a positive feedback [15,16]. The formation of the von Kármán vortex street at the end of the L_1 wake region significantly elevates the turbulence level, which may inhibit deposition. Beyond this point the velocity begins to recover back to the free stream value U_0.

Although several studies have contributed to the description of flow and deposition near an individual patch of vegetation, relatively few studies have investigated the interaction between two patches placed in close proximity to one another. The interaction between two developing wakes makes the flow field behind a pair of patches significantly more complex than that near a single patch. In the relatively simple case of two side-by-side circular patches separated by a gap, the flow is accelerated next to and in between the patches for all gap widths [7, 17]. This flow acceleration would tend to promote erosion and thereby inhibit the lateral growth of the patches. The wake in line with and immediately downstream of each individual patch is similar to that observed behind a single isolated patch, creating conditions that favor the deposition of fine material and, consequently, patch expansion in the streamwise direction in line with the individual patches [17]. Further downstream, the two wakes merge, producing a velocity minimum that promotes deposition on the centerline between the patches, but at some distance removed from the patches. Meire et al. [17] argue that this secondary deposition region may promote the growth of vegetation on the centerline between the patches, which in turn could diminish the flow between the patches, ultimately producing conditions favorable for the two patches to merge.

In this paper we build on the work of Meire et al. [17] by considering a wider range of two-patch configurations. In particular, the patch spacing was varied in both the transverse and longitudinal direction, denoted by T and L, respectively, as in Fig. 1. This is an important refinement, because in very few cases will the oncoming flow be perfectly aligned with the patches, i.e. $L = 0$, as assumed by Meire et al. [17]. A numerical model was used to explore how the patch spacing impacts the shape of the wake behind each patch, and the modeled velocity

81　field was used to infer possible deposition and growth patterns. Using the results for pairs of
82　patches, we infer how initial patch spacing might influence landscape development.

83

2. Modeling Approach

85　　　This study considered emergent vegetation, for which flow diversion occurs
86　predominantly in the horizontal plane. In particular, previous experimental studies using similar
87　flow and patch configurations showed that three-dimensional effects associated with the bottom
88　boundary-layer were of second order with regard to wake structure [18]. Subsequently, we have
89　chosen a two-dimensional model, representing the streamwise and transverse coordinates,
90　respectively (Fig. 1). In this study the x-axis pointed in the direction of flow with $x = 0$ at the
91　upstream edge of the patches, and the y-axis was in the transverse direction, with $y = 0$ at the
92　center of the transverse gap between the patches. The longitudinal (L) and transverse (T)
93　spacing between the patches was measured between the patch centers. The velocity (u, v)
94　corresponded to (x, y), respectively. The individual stems within a patch were represented by
95　solid cylinders of diameter d, placed with stem density n [cylinders/cm^2]. This produced a
96　frontal area per volume of $a = nd$, and a solid volume fraction $\phi = (\pi/4)\,ad$.
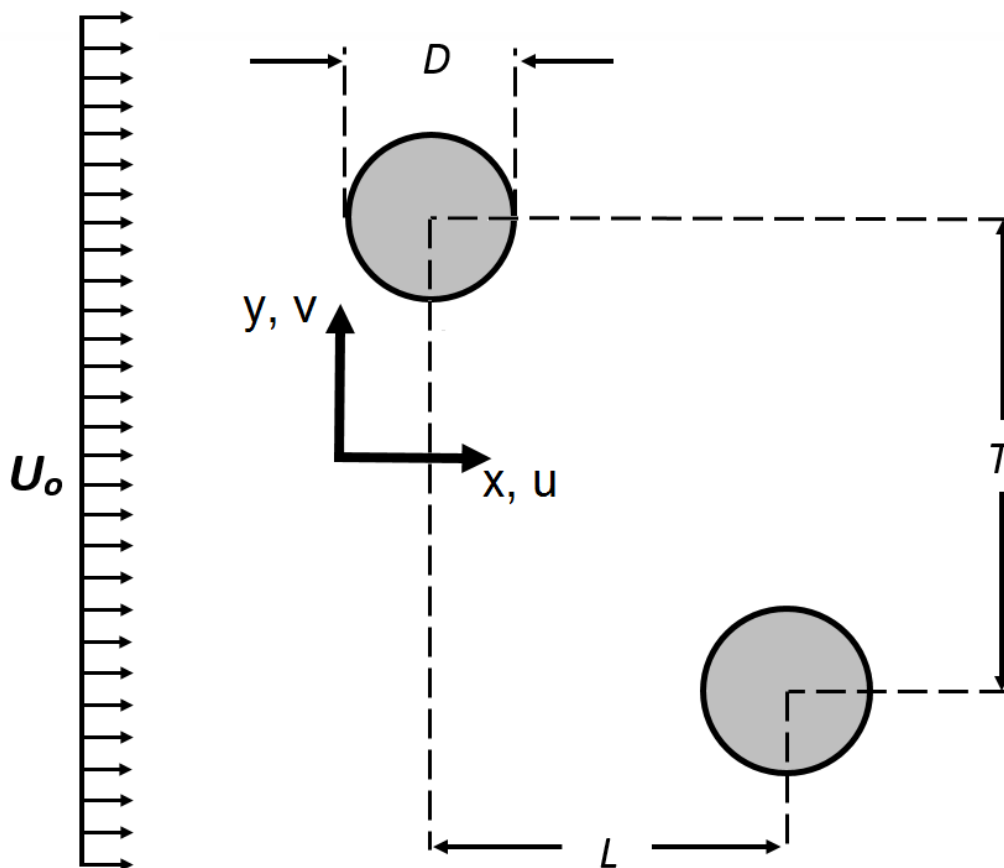
97
98　**Fig. 1** Definition sketch for two circular patches (grey circles) of equal diameter, D. L is the longitudinal spacing and
99　T is the transverse spacing, both measured between the centers of each patch. U_0 is the uniform inlet velocity set to
100　9.5 cm s^{-1} for these experiments.

101　　　Numerical experiments were carried out for 46 patch arrangements defined by eight
102　different values of T/D between 1 and 8, and nine different values of L/D between 0 and 25. The

103 specific combinations of *T/D* and *L/D* are shown in Figure 2. Each patch had a diameter *D* = 22
104 cm, and was composed of 45 rigid cylinders of diameter *d* = 1.2 cm in a staggered arrangement,
105 producing a solid volume fraction of $\phi \approx$ 10% and a frontal area per volume *a* = 0.13 cm^{-1}. The
106 numerical experiments were conducted with U_0 = 9.5 cm/s. To reduce the influence of the inlet,
107 the upstream patch was placed 3 m ($\approx$ 14*D*) downstream from the channel inlet. The
108 computational flow domain chosen spans 45*D* (to 60*D*) in the streamwise direction and 20*D* in
109 the spanwise direction. The blockage ratio, *B*, i.e., the ratio of the total obstructed width (2D) to
110 the channel width (*W* = 25*D*) was 0.08. Since *B* << 1, the impact of the channel walls was low:
111 preliminary simulations showed that, for channel widths of 15*D* and 20*D*, the difference in the
112 velocity for any point was less than 5% (tested specifically for *L/D* = 0 and *T/D* = 1.5).
113   In order to provide a baseline for comparison, six simulations with a single patch were
114 also performed. In these runs the center of the single patch was placed at the same position as
115 the upstream patch within the pair. Specifically, single patch controls were run for *x* = 0.5*D* and
116 *y* = 0.5*D*, 0.545*D*, 0.625*D*, 0.75*D*, 1*D*, and 1.5*D*, corresponding to the two-patch cases *T/D* = 1,
117 1.09, 1.25, 1.5, 2, and 3.
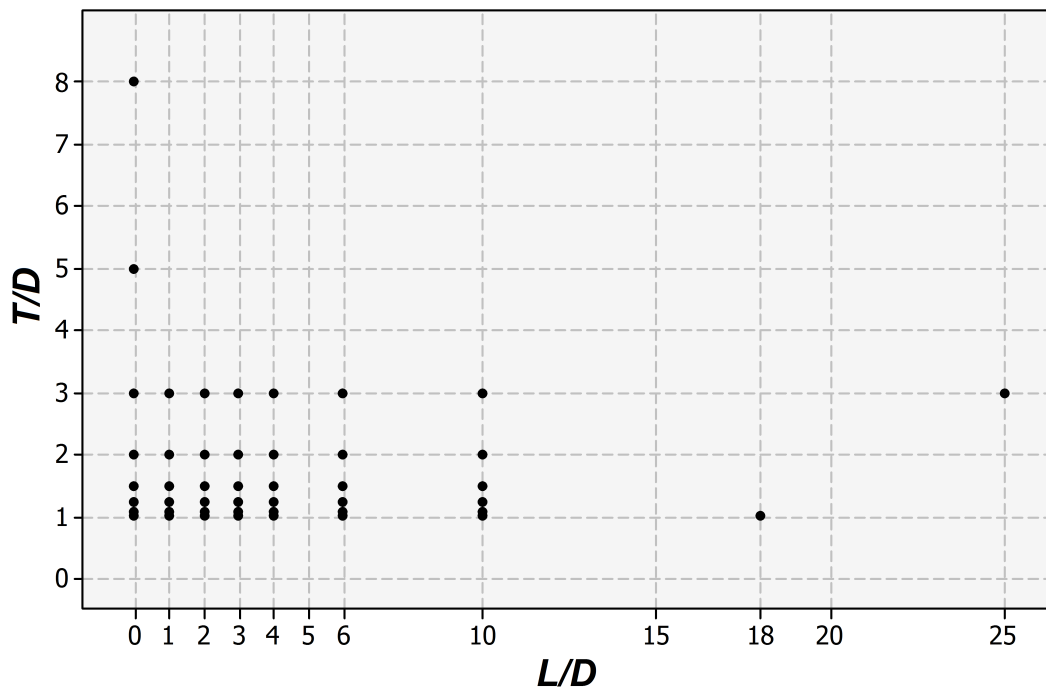
118
119 **Fig. 2** The 46 two-patch arrangements consider in this study. The center-to-center longitudinal spacing (*L*) and
120 transverse (*T*) spacing were both varied.

121   Simulations were carried out using the commercial CFD (Computational Fluid
122 Dynamics) code FLUENT$^{®}$. This code uses the finite volume method for the spatial
123 discretization of the domain. The governing equations are integrated over each control volume,
124 such that mass and momentum are conserved, in a discrete sense, for each control volume. The
125 simulations in this study were performed using the two-dimensional steady-state RANS
126 (Reynolds Averaged Navier Stokes) equations with a k–ε model.
127   Considering a steady flow of an incompressible and homogeneous fluid, the Reynolds-
128 averaged equations for conservation of mass and momentum are given by:

$$\frac{\partial u_i}{\partial x_i} = 0$$

$$\frac{\partial u_j u_i}{\partial x_j} = -\frac{1}{\rho}\frac{\partial p}{\partial x_i} + \nu\frac{\partial^2 u_i}{\partial x_j \partial x_j} - \frac{\partial \overline{u_i' u_j'}}{\partial x_j}$$

129   where i or j = 1 or 2; x_1 and x_2 denote the streamwise (x) and cross-stream (y) directions
130   respectively; u_1 and u_2 are the corresponding mean velocity components (i.e., $u_1 = u$ and $u_2 = v$).
131     $\overline{u_i' u_j'}$ is the Reynolds stress component, where u' denotes the fluctuating part of the velocity; p is
132   the pressure; and ρ is the fluid density. For the calculation of the Reynolds stresses, the
133   assumption of Boussinesq's approximation is used

$$\overline{u_i' u_j'} = \frac{\mu_t}{\rho}\left(\frac{\partial u_i}{\partial x_j} + \frac{\partial u_j}{\partial x_i}\right) - \frac{2}{3}k\delta_{ij}$$

134   where μ_t is the turbulent viscosity, δ_{ij} the Kronecker delta and k is the turbulent kinetic energy
135   per unit mass, given by

$$k = \frac{1}{2}\left(\overline{u_1^2} + \overline{u_2^2}\right)$$

136   Along with the Boussinesq approximation, the following definition of the eddy viscosity is used

$$\mu_t = \rho c_\mu \frac{k^2}{\varepsilon}$$

137   where c_{μ} is an empirical constant and ε is the energy dissipation rate given by the following
138   equation

$$\varepsilon = \frac{k^{\frac{3}{2}}}{S}$$

139   where S is the length scale involved. The distributions of k and ε are calculated from the
140   following transport equations

$$\frac{\partial \rho u_j k}{\partial x_j} = \frac{\partial}{\partial x_j}\left(\frac{\mu_t}{\sigma_k}\frac{\partial k}{\partial x_j}\right) + G - \rho\varepsilon$$

$$\frac{\partial \rho u_j \varepsilon}{\partial x_j} = \frac{\partial}{\partial x_j}\left(\frac{\mu_t}{\sigma_\varepsilon}\frac{\partial \varepsilon}{\partial x_j}\right) + c_1\frac{\varepsilon}{k}G - \rho c_2\frac{\varepsilon^2}{k}$$

141   where G represents the generation of turbulence kinetic energy due to the mean velocity
142   gradients

$$G = \mu_t\left(\frac{\partial u_i}{\partial x_j} + \frac{\partial u_j}{\partial x_i}\right)\frac{\partial u_i}{\partial x_j}$$

143   The standard values of the constants $c_\mu = 0.09$, $c_1 = 1.44$, $c_2 = 1.92$, $\sigma_k = 1.0$ and $\sigma_\varepsilon = 1.3$ are
144   used in the present computations.

145   As already mentioned, two-dimensional simulations were used in this study as they are
146   able to capture the flow features that are important for the present goal. Fluent, CFD numerical
147   code used in this study, use the finite control-volume method for the spatial discretization of the
148   domain. Hence, in the two-dimensional simulations the volume is the computational domain in
149   the xy plane multiplied by a unit depth (in the z direction). Pressure-velocity coupling was
150   achieved in some simulations using the SIMPLE (Semi-Implicit Method for Pressure-Linked
151   Equations) and in other simulations a combination of the SIMPLE and coupled pressure-based
152   algorithms. In most of the cases, the simulations converged only using the SIMPLE method. In
153   a few cases we changed from SIMPLE to coupled algorithm to reach the convergence of the
154   solution. A second order upwind scheme was used for spatial discretization of the flow
155   equations. Details of the governing equations, turbulence model, and algorithms can be found in
156   the FLUENT® user's guide [19].

157   The full domain and zoomed-in views of the numerical grid for $L/D = 1$ and $T/D = 2$ are
158   shown in Figure 3. The grid had a finer spacing in regions of larger gradients (near the wall, the
159   patch, and the wake) and coarser spacing in the regions of low velocity gradients. In addition,
160   the grid was a block-structured grid composed of Cartesian H-grid blocks, which were uniform
161   in the horizontal plane, and O-grid blocks, which were stretched towards the cylinders. The
162   present meshing method has been previously applied with success for flows around cylinders
163   (see, for example, Stoesser et al. [20]). A grid independency test was performed to ensure the
164   quality of our CFD simulations. Three progressively finer grids were employed: a coarser grid,
165   with 799600 elements; a medium grid, with 1131000 elements; and a fine grid, with 1605000
166   elements.
167   The cylinders into the patch were arranged in a square array. The array was drawn
168   inside a circle with diameter of 22cm that represents the boundary of the patch. The array have a
169   square form divided in 49 (7x7) smaller squares with 3cmx3cm. The small squares in the array
170   were filled with the stems. The stems and small squares are all concentric. Finally the 45 stems
171   were disposed symmetrically into the array and for this reason there are no stems at the array
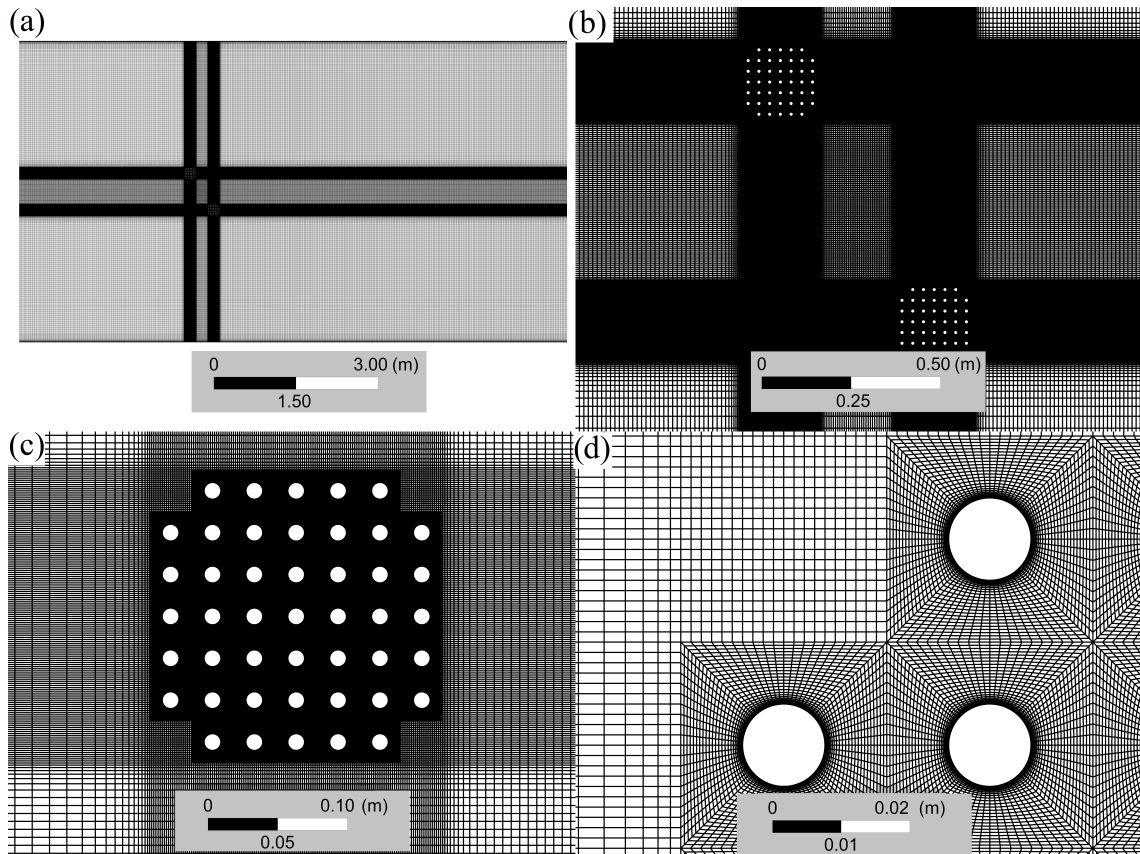172   corners (See Fig. 3c).

Fig. 3 Computational grid for the $L/D = 1$ and $T/D = 2$ case: (a) entire computational domain; (b) close-up view near the 2 patches; (c) close-up view near one patch; and (d) close-up view near the cylinders.

Boundary conditions were defined at the borders of the computation domain. A uniform flow was imposed at the inlet, with streamwise velocity $u = U_0$ and transverse velocity $v = 0$. At the outlet an average static reference pressure of 0 Pa was specified. The zero-pressure outlet boundary condition has been widely used to calculate the flow around bluff bodies (see e.g. Tian et al. [21]). A no-slip boundary condition was applied at the cylinder edges and the channel walls. Symmetry conditions were applied at the bottom and the surface of the channel.

The numerical model was validated using experimental measurements near a single patch in a laboratory channel [12]. The simulations represented a 10-m long and 1.2-m wide channel with imposed inflow velocity $U_0 = 9.5$ cm/s. A single circular patch of diameter $D = 22$ cm was placed 3m downstream from the channel entrance. To simplify the computational mesh, the computational cylinders were arranged into a square array, rather than a circular array used by Zong and Nepf [12]. This simplification is justified by experiments carried out by Vandenbruwaene et al. [7], who found that the flow field near square and circular arrays of the same diameter and stem density were very similar. The computational patch had 35 rigid cylinders ($n = 0.1$ cylinders cm^{-2}) of diameter 0.6 cm, producing a solid volume fraction of $\phi \approx 0.03$, which is the same used by Zong and Nepf [12]. The frontal area per volume was $a = nd \approx 0.06$ cm^{-1}. Streamwise profiles of time-mean velocity along the centerline of the patch show that the maximum difference between numerical and experimental results was 6% or less of the experimental measurement (Fig. 4). Figure 4 reveals that all three grids predictions were similar. Due to the limitation of available computational time, the coarse mesh was selected. It is important to note, as observed from comparison between experimental and numerical results in Figure 4, that the most significant steady wake characteristics can be captured with a steady RANS simulation.
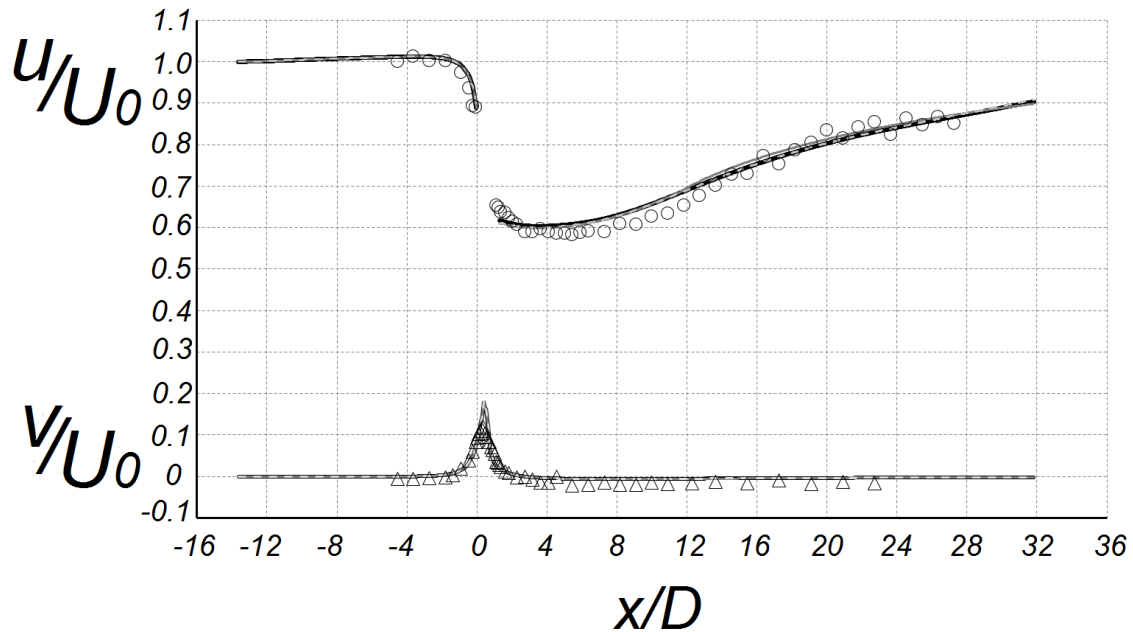
Fig.4 Comparison of the simulated time-mean streamwise velocity (u) along the centerline of the patch and transversal velocity (v) along the line $y=D/2$ with the experiment of Zong and Nepf (2011), open circles and open triangles for u and v, respectively. The boundaries of the patches lies between $0 < x/D < 1$. The maximum difference between numerical and experimental results was 6%. In both the numerical and physical experiment, the patch width was $D = 22$ cm, and the patch solid volume fraction was $\phi = 0.03$. Coarse grid, with 799600 elements (solid black lines); medium grid, with 1131000 elements (solid gray lines); fine grid, with 1605000 elements (dashed gray lines).

Regions of deposition are commonly associated with regions of diminished velocity [17, 22]. For example, the effect of velocity on deposition is illustrated by Hjulström's diagram [23], which relates deposition to velocity and particle size. Sediment is deposited when the velocity falls below the minimum velocity required to keep the particle in motion, which we call the threshold velocity. The threshold velocity is a function of sediment size, with smaller values associated with smaller grains. We used the threshold velocity to define the regions within which enhanced deposition would occur in the wake of the individual patches and patch pairs. Recognizing that the threshold velocity will depend on sediment size, we considered two thresholds, $u/U_0 < 0.7$ and 0.5, representing coarser and finer material, respectively. Although we cannot connect these velocities to specific sediment sizes, they provide an exploratory test of how threshold velocity impacts the areal extent of enhanced deposition. In addition, the higher threshold ($u/U_0 < 0.7$) is correlated with the regions of enhanced net deposition observed in both Chen et al [16] and Meire et al. [17].

3.   Results and Discussion

3.1 Flow pattern around a single patch

The velocity distribution for a single patch ($D = 22$ cm, $a = 0.13$ cm^{-1}) is shown in Fig. 5. The diversion of flow began at $L_0 = 1.45D$ upstream of the patch, with L_0 defined as the distance upstream of the patch at which $\left|\frac{\partial(u/U_0)}{\partial(x/D)}\right| > 0.05$, which is consistent with results presented in Rominger and Nepf [11] of $L_0 = 2.0$ (± 0.4) D and Zong and Nepf [12] of $L_0 \approx 1D$. The diversion of flow away from the vegetation patch led to acceleration along the vegetation edge, which is apparent in Fig. 5 as lobes of lighter shading on each side of the patch. Flow continued to divert laterally even within the patch, resulting in an area of low velocity directly

229 behind the patch, consistent with previous studies [9, 16]. The velocity directly downstream of
230 the patch was $U_e = 0.40U_o$.

231   There was no recirculation zone behind the patch (specifically, no region of negative
232 velocity), which is in agreement with Chen et al. [16], who note that there is no recirculation
233 zone behind low-flow blockage patches ($C_D aD < 4$).

234   The region of low velocity behind the patch separated two regions of enhanced velocity,
235 creating a shear layer on either side of the wake. The region of diminished velocity was
236 maintained over a distance L_1 measured from the back of the patch. The wake length, L_1, was
237 defined as the distance along the patch centerline from the end of the patch to the point where
238 the velocity began to increase. The dimensionless wake length obtained for our simulations was
239 $L_1/D \approx 4.1$.
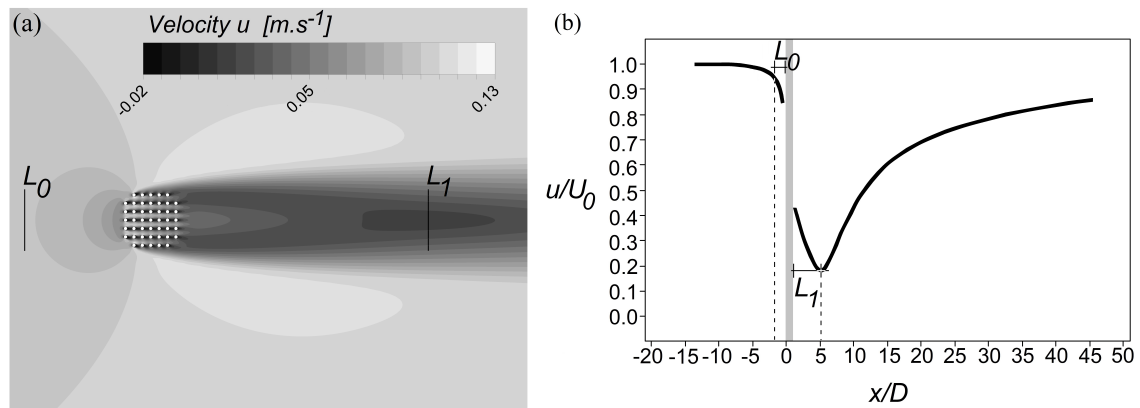
240
241 **Fig. 5** (a) Contour map of streamwise velocity (u) for a single patch of diameter $D = 22$cm, $a = 0.13$ cm^{-1} and flow
242 blockage $aD = 2.86$. The center of the patch is at $x = 0.5D$, $y = 0.75D$; (b) streamwise velocity (u) along the patch
243 centerline noting the length-scales L_0 and L_1.

244 **3.2 Flow pattern around two patches**

245   The presence of a neighboring patch changes the wake structure, relative to that
246 observed for an isolated patch (discussed in 3.1). We used the wake length, L_1, to explore the
247 influence of a neighboring patch for different lateral (L) and transverse (T) distances (Fig. 6).
248 The superscripts u and d indicate, respectively, the upstream patch (L_1^u) and the downstream
249 patch (L_1^d). The value for an isolated, single patch will remain as L_1. Three different patterns for
250 L_1 were identified, depending on the patch spacing, L/D and T/D: (i) single patch behavior, in
251 which each of the two patches produced a wake that was close to that produced by a single,
252 isolated patch. This behavior was defined by the following limits: $0.9 \leq L_1^u/L_1^d \leq 1.1$, $0.9 \leq$
253 $L_1^u/L_1 \leq 1.1$ and $0.9 \leq L_1^d/L_1 \leq 1.1$; (ii) biased flow behavior, in which the lengths of the two
254 wakes differed by more than 10% ($0 \leq L_1^u/L_1^d \leq 0.9$); (iii) diminished wake behavior, in which
255 the lengths of the two wakes are equal, but smaller than the length behind an isolated patch (0.9
256 $\leq L_1^u/L_1^d \leq 1.1$ and $L_1^u/L_1 \leq 0.9$ and $L_1^d/L_1 \leq 0.9$). These three flow patterns are now examined
257 in more detail.
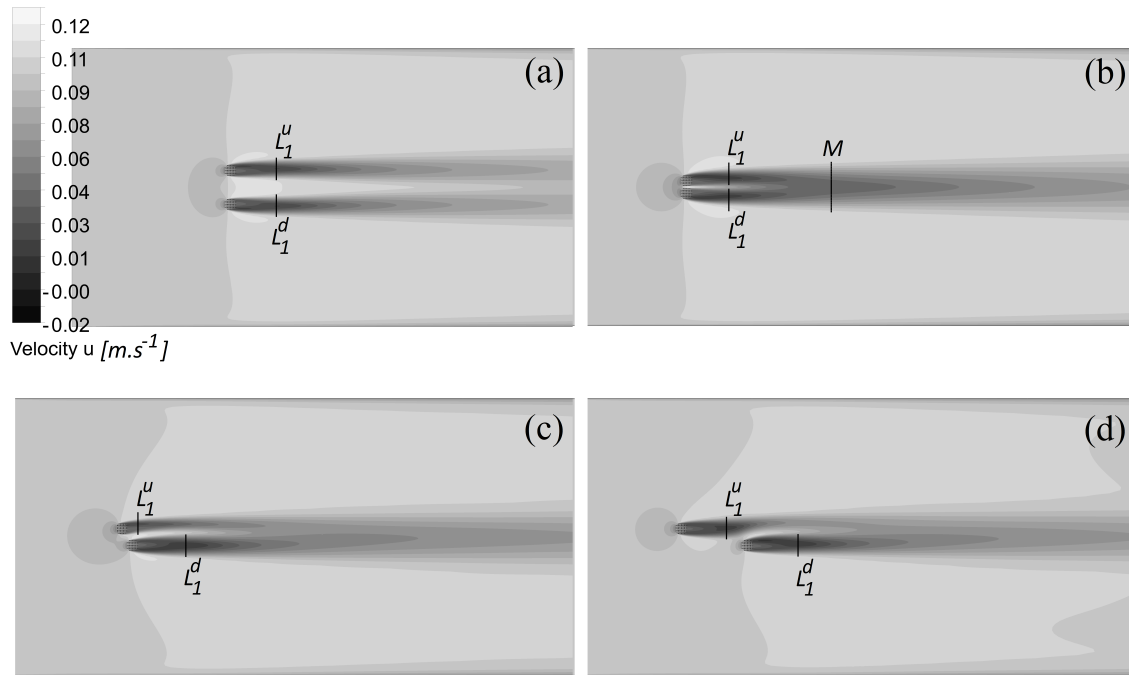
Fig. 6 *u*-velocity contours for (a) $L/D = 0$, $T/D = 3$ (single patch behavior); (b) $L/D = 0$, $T/D = 1.09$ (diminished wake behavior); (c) $L/D = 1$, $T/D = 1.5$ (biased flow behavior); (d) $L/D = 6$, $T/D = 1.5$ (biased flow behavior). M marks the longitudinal position at which the two wakes merge into one, as indicated by a velocity minimum in the longitudinal transect along the centerline between the two patches (M could be only defined for the case in Fig. 6b).

3.3   Flow pattern around side-by-side patches, *L/D* = 0

Figure 6a and 6b show *u*-velocity distributions for two cases ($T/D = 3$; $T/D = 1.09$) in a side-by-side arrangement ($L/D = 0$). The upstream adjustment length (L_0) was a weak function of lateral spacing, *T*, with $L_0 = 1.92D$ for $T/D = 1.09$ and $L_0 = 1.44D$ for $T/D = 2$. Recall that $L_0/D = 1.45$ for single, isolated patch (Fig. 5). The values of L_0 observed for these side-by-side arrangements were close to those measured by Meire et al. [17] of $L_0 = 1.7$ ($\pm$ 0.2) *D* over a range of spacing ($T/D = 1$ to 1.6, $L/D = 0$). Further, the values of L_0 observed for the side-by-side arrangement agreed within uncertainty with Rominger and Nepf [11], who observed $L_0 = 2.0 \pm 0.4$ *D* for individual patches. Thus, although our simulation suggested that L_0 increased by 30% as the spacing decreased to nearly zero ($T/D = 1.09$), the values were all within the range observed for isolated patches, which suggests that there was no upstream interaction, i.e. the presence of a neighboring patch did not significantly alter the distance upstream at which flow begins to adjust to each patch.

For $L/D = 0$, the flow pattern was symmetric about $y = 0$ such that the near wake length-scale (L_1) behind each patch was the same (Fig. 6a and 6b), but in these two cases was smaller than that observed for an isolated patch ($L_1/D = 4.1$), which we call diminished wake behavior. In addition, L_1 was a function of patch-spacing *T*. Specifically, $L_1/D = 3.40$ at $T/D = 1.09$ and $L_1/D = 3.75$ at $T/D = 3.0$, i.e. as the patch-spacing increased the wake length-scale approached that of an isolated patch, which makes physical sense. The parameter range (T/D) on which diminished wake behavior occurs is discussed in more detail below in the context of Fig. 8.

The result that L_1 was shortened in a side-by-side configuration ($L/D = 0$) differed from Meire et al. [17], who observed that L_1 for a pair of side-by-side patches was not significantly altered from that of an isolated patch. This difference may be explained by the resolution of the Meire measurements. In the Meire study the longitudinal distance between measurement points was 0.55D, a distance that roughly encompasses the variation observed in this study (3.4*D* to

288   4.1*D*). Finally, for *L/D* = 0 flow acceleration between the patches was always present, even for

289   *T/D* = 1, which is consistent with both Meire et al. [17] and Vandenbruwaene et al. [11].

290   Downstream from a pair of side-by-side patches, the flow field evolved in the

291   streamwise direction from two side-by-side wakes to a single merged wake (e.g. *L/D* = 0, *T/D* =

292   1.5, Fig. 7). Close to the patch pair (e.g. *x/D* =2) the profile showed two distinct wakes with

293   local minimum velocity in-line with the individual patches and a maximum velocity on the

294   centerline between the patches (*y* = 0). Farther downstream (x/D > 2), the centerline (*y*=0)

295   velocity declined as the individual wakes merged, reaching the form of a single wake at *x/D* =

296   19.5. At this point, which we call the merging point *M*, the centerline velocity reached a

297   minimum. Beyond this point (*x/D* ≥ 19.5) the wake resembled that of a larger, single patch of

298   scale (*D+L*) with the minimum velocity in the lateral transect occurring at the centerline

299   between the two patches. The wake merger (*M*) and centerline minimum velocity occurred

300   closer to the patches as patch lateral space (*T/D*) decreased, consistent with the observations of

301   Meire et al [17]. For example, the wake merger position (*M*) is visible within the frame for *T/D*

302   = 1.09 (Fig. 6b), but occurs beyond the end of the frame for *T/D* = 3 (Fig. 6a). The merger

303   position (*M*) and associated centerline velocity minimum have been shown experimentally to

304   promote a local region of enhanced deposition on the centerline between the two patches.

305
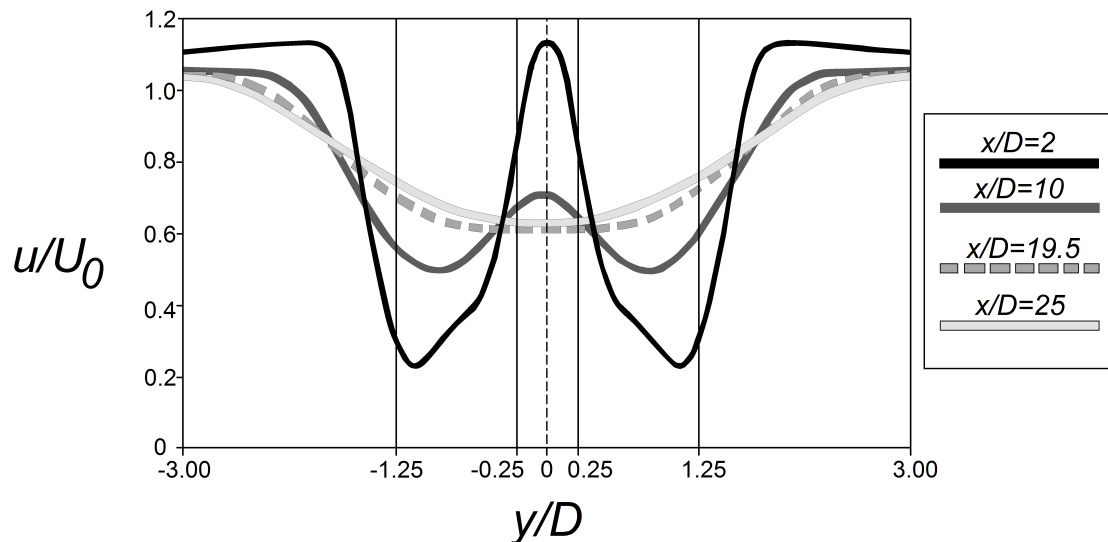
306   **Fig. 7** Lateral profiles of streamwise velocity (u) for *T/D* = 1.5 and *L/D* = 0 (side-by-side configuration). The dashed,

307   vertical line indicates the centerline between the patches (*y* = 0), and the solid vertical lines represent the edges of the

308   patches. At *x/D* = 2 and 10, two distinct wakes were visible, with minimum velocity aligned with the centerline of

309   each patch. At *x/D* = 19.5 and 25 the individual wakes have merged to form a wake that resembles that of a single

310   object of total width (*D+L*), with a minimum velocity at the centerline between the two patches (y = 0).

311   **3.4   Flow pattern around two staggered patches, *L/D* > 0.**

312   Figure 6c and 6d illustrate two staggered configurations (*L/D* > 0). When the

313   neighboring patches were staggered, the flow through the gap between the patches was

314   deflected laterally toward the upstream patch, and this cut off the wake development of the

315   upstream patch. As a result, the wake length of the upstream patch (L_1^u) was smaller than that

316   for an isolated patch (L_1). The wake behind the downstream patch was essentially the same as

317   an isolated patch (within 10%). As *L/D* increased, the deflection of gap flow decreased, and the

318   upstream wake lengthened (L_1^u increased), until at *L/D* = 6, the upstream and downstream

319   values for L_1 were equal within 10%. This suggests that a downstream patch that occurs within

320   6*D* of an upstream neighbor can produce a negative feedback for the upstream patch by

diminishing the length of the near wake, from which we infer the length-scale of enhanced
deposition and potential growth will also be diminished.
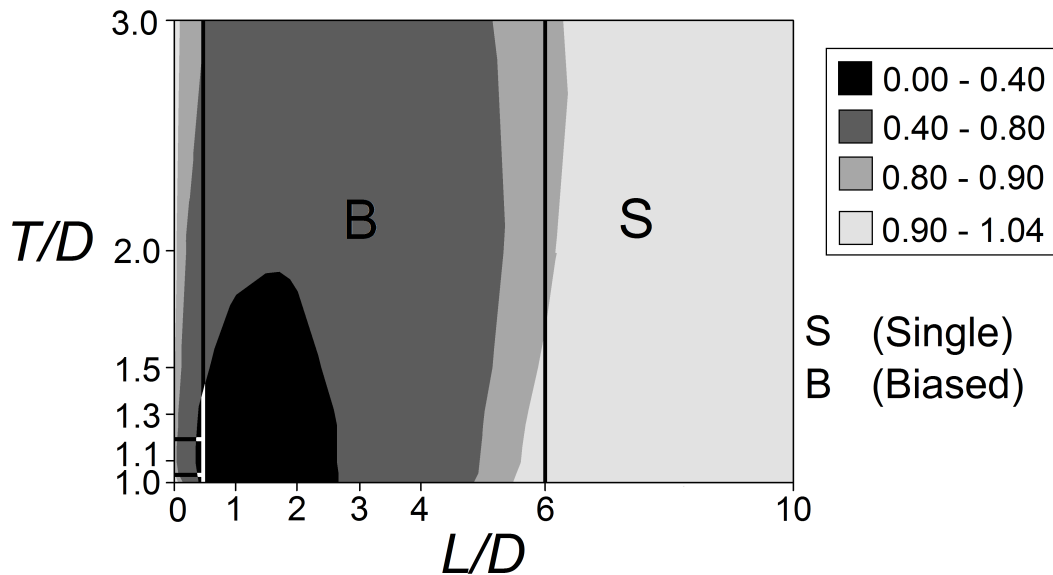
Fig. 8 Ratio of upstream to downstream wake length-scale, L_1^u/L_1^d, as a function of L/D and T/D. Regions of biased flow behavior (B) and single patch behavior (S) are marked. The boundaries were drawn at the half distance between simulated values of L/D and T/D. The diminished wake behavior was only observed for side-by-side patches ($L/D = 0$) over the range $T/D = 1.09$ to 1.25. For $L/D = 0$, $T/D > 1.25$, single patch behavior was observed.

The variation in the wake length-scale ratio L_1^u/L_1^d over the full range of lateral (L/D) and transverse (T/D) spacing is shown in Figure 8. These values were used to define the classes of wake behavior, as discussed in the previous paragraphs. In particular, the biased flow (B) and single patch (S) behavior is noted in Figure 8 with boundaries drawn at half the distance between the simulated values of L/D or T/D at which the transition was observed. We first consider the side-by-side configurations with $L/D = 0$. If the patches were spaced sufficiently far apart ($T/D > 1.25$), they behaved as two independent patches, with L_1 of each patch comparable to that of an isolated patch, i.e. single patch behavior. If the patches were at an intermediate spacing ($1.09 \leq T/D \leq 1.25$), the lengths of the two wakes are equal, but smaller than the length behind a single patch (diminished wake behavior). If the patches were touching ($T/D = 1$), single patch behavior was again observed ($L_1^u = L_1^d = L_1$).

For $L/D > 0$, when the patches were far from one other ($L/D > 6$), they exhibited single patch behavior (marked S in Fig. 8), i.e. there was no influence between the patches and $L_1^u = L_1^d = L_1$. If the patches were closer ($0 < L/D < 6$), biased flow occurred and the upstream wake was significantly shorter than the downstream wake and decreased in length as the spacing (L/D) decreased. The minimum value of $L_1^u/L_1^d = 0$ (i.e. the upstream patch had no near wake region) occurred for $L/D = 1$ and $T/D = 1$ to 1.25.

3.5 Implied Deposition pattern

This section explores the possible influence of the velocity field on deposition patterns by delineating regions of potential net deposition based on two velocity thresholds, $u/U_0 < 0.5$ and 0.7. The potential deposition area was defined as the area within which the local velocity was below the chosen threshold. The deposition area for a single patch, A_1, for $u/U_0 < 0.5$ and

350 0.7, was $9.9D^2$ and $22.7D^2$, respectively, and was not a function of patch position (Fig. 9). These
351 areas will be used as the reference values as we explore the interaction of two patches.
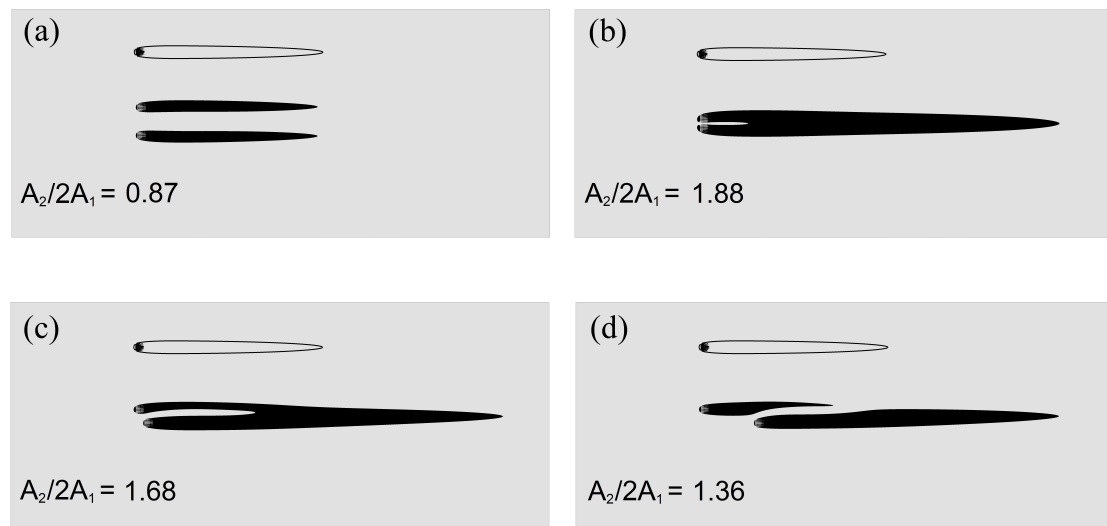
(a) L_1

(b) L_1

352
353 **Fig. 9** The deposition area for a single patch (A_1) is identified by the black color for two threshold velocities: (a) u/U_0
354 < 0.7, $A_1 = 22.7D^2$; (b) $u/U_0 < 0.5$, $A_1 = 9.9D^2$.

355   For pairs of patches, the deposition area behind the upstream and downstream patch was
356 denoted A_u and A_d, respectively, and the sum was defined as $A_2 = A_u + A_d$. Different deposition
357 patterns were identified from the simulations, corresponding to the different flow patterns
358 identified above. First, for single patch flow behavior, both patches have the same (within a
359 10% margin) deposition area as an isolated patch. That is, $0.9 \le A_u/A_1 \le 1.1$; $0.9 \le A_d/A_1 \le 1.1$.
360 This deposition pattern occurred when the two patches were far apart, so that no interaction
361 between the two patches occurred, resulting in a single deposition zone behind each patch with
362 an area the same as an isolated patch ($A_2/2A_1 \approx 1$). In this case, the presence of a neighboring
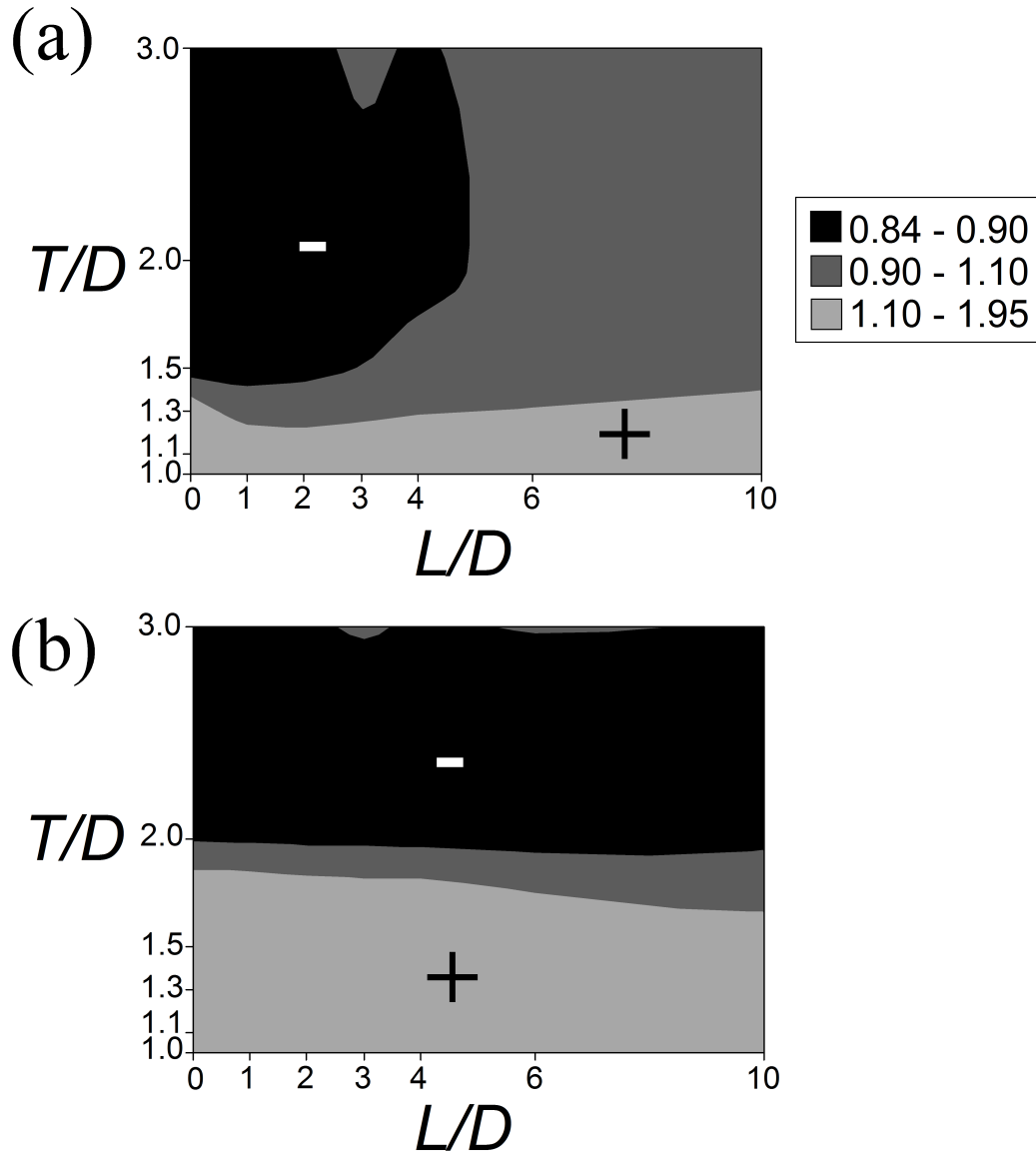363 patch produced no feedback.
364   Second, when the two patches were located side-by-side ($L/D = 0$), A_u and A_d are equal
365 (within 10%), but different from the area behind a single patch ($0.9 \le A_u/A_d \le 1.1$; $A_d/A_1 \le 0.9$
366 or $A_d/A_1 \ge 1.1$; $A_u/A_1 \le 0.9$ or $A_u/A_1 \ge 1.1$). Two types of deposition pattern were observed for
367 patches in a side-by-side configuration ($L/D = 0$): with a secondary deposition zone (Fig. 10b
368 and 11b) and without a secondary deposition zone (Fig. 10a and 11a). In both cases the total
369 deposition area with two patches (A_2) was different from that of two isolated patches ($A_2/2A_1 \neq$
370 1). When there was no secondary deposition zone (Fig. 10a and 11a), the deposition area of the
371 two patches were equal, but less than the area behind a single patch, so that $A_2/2A_1 < 1$.
372 Neighboring patches in this configuration produced a negative feedback, because a neighboring
373 patch diminished the overall deposition, compared to two isolated patches. When a secondary
374 deposition zone was present, the total deposition area of the two patches was greater than two
375 individual patches ($A_2/2A_1 > 1$, Fig. 10b and 11b). Neighboring patches in this configuration
376 provided a positive feedback, because the neighboring patch enhanced the overall deposition
377 and potential for new growth. The leading edge of the secondary deposition zone moved closer
378 to the patches as T decreased, consistent with the experimental deposition patterns obtained by
379 Meire et al. [17]. As suggested by Meire et al. [17], if the zones of secondary deposition
380 promote growth, the new vegetation on the centerline could block flow on the centerline,
381 eventually leading to a merger of the original patches into a larger vegetated structure.
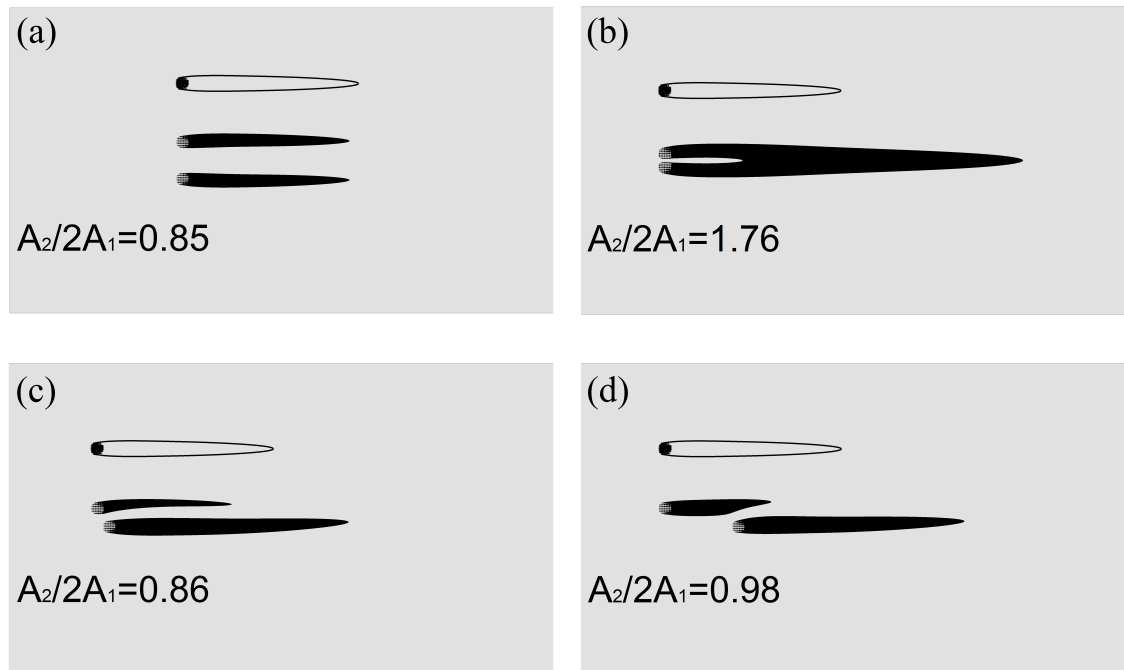
Fig. 10 Deposition areas identified by the black color for $u/U_0 < 0.5$. A_1 is the deposition area produced by an isolated patch and A_2 is the total deposition area created with two patches. (a) $L/D = 0$, $T/D = 3$; (b) $L/D = 0$, $T/D = 1.09$; (c) $L/D = 1$, $T/D = 1.5$; (d) $L/D = 6$, $T/D = 1.5$. Each subplot indicates the single-patch deposition area with an open contour. The total deposition area with two patches, A_2, is compared to that expected for two isolated patches ($2A_1$). When $A_2/2A_1 > 1$, the neighboring patches provide a positive feedback to growth by creating a larger footprint of deposition than occurs for two isolated patches. When $A_2/2A_1 < 1$, the neighboring patches provide a negative feedback by diminishing the footprint of deposition, compared to two isolated patches.

Fig. 11 Deposition areas identified by the black color for $u/U_0 < 0.7$. A_1 is the deposition area produced by an isolated patch and A_2 is the total deposition area created with two patches. (a) $L/D = 0$, $T/D = 3$; (b) $L/D = 0$, $T/D = 1.09$; (c) $L/D = 1$, $T/D = 1.5$; (d) $L/D = 6$, $T/D = 1.5$. Each subplot indicates the single-patch deposition area with an open contour. The total deposition area with two patches, A_2, is compared to that expected for two isolated patches ($2A_1$). When $A_2/2A_1 > 1$, the neighboring patches provide a positive feedback to growth by creating a larger footprint of deposition than occurs for two isolated patches. When $A_2/2A_1 < 1$, the neighboring patches provide a negative feedback by diminishing the footprint of deposition, compared to two isolated patches.

Fig. 12 Dependence on *L/D* and *T/D* of the nondimensional deposition area, $A_2/2A_1$ for deposition defined by two velocity thresholds: (a) $u/U_0 < 0.5$; (b) $u/U_0 < 0.7$. The plus ("+") and minus ("-") signs indicate, respectively, positive and negative feedbacks due to the presence of a neighboring patch.

Third, for cases with biased flow behavior, two deposition patterns were observed: with a secondary deposition zone (Fig. 11c) and without a secondary deposition zone (Fig. 10c, 10d and 11d). In the later case (11d), the deposition zone behind the upstream patch was smaller than that behind an isolated patch ($A_u < A_1$), so that the downstream neighbor provided a negative feedback to growth for the upstream patch. In contrast, there was an increase in deposition area behind the downstream patch compared to a single patch ($A_d > A_1$), i.e. an upstream neighbor enhanced (positive feedback) the growth potential of the downstream patch.

Figure 12 summarizes the tendencies for positive (light grey) and negative (black) feedbacks associated with different patch-to-patch spacing for both velocity thresholds. We first consider the $u/U_0 < 0.5$ threshold (top subplot). For the side-by-side configurations ($L = 0$), unless the patches were nearly touching ($T/D < 1.5$), neighboring patches produced a negative feedback ($A_2/2A_1 < 0.9$). The negative feedback was observed for lateral spacing as large as $T/D = 8$, but for larger spacing we expect the deposition to return to single-patch behavior ($A_2/2A_1 = 1.0 \pm 0.1$). On the other hand, when the patches had a small lateral spacing ($T/D < 1.3$), a

416　positive feedback ($A_2/2A_1 > 1.1$) was observed for all longitudinal spacing considered (grey
417　region along x-axis). The maximum feedback ($A_2/2A_1 = 1.95$) occurred at ($L/D = 0$, $T/D = 1$).
418　For patches separated by more than $L/D = 5$ and $T/D = 1.5$, there was no feedback, and the
419　deposition area was essential that same as that produced by two isolated patches ($A_2/2A_1 = 1.0 \pm$
420　0.1, medium grey region in Fig. 12a). When we considered a higher threshold velocity ($u/U_0 <$
421　0.7, Fig. 12b), both the positive and negative patch interactions became stronger, i.e. positive
422　and negative feedbacks both occurred over a larger L-T parameter space. The expansion of the
423　positive feedback region occurred because with a higher threshold velocity weaker patch
424　interactions are needed to depress the velocity below this threshold, and these weaker
425　interactions can occur at larger patch spacing. The enlargement of the negative feedback
426　parameter space is related to the fact that the deposition area of an isolate patch (A_1) increases
427　(due to a higher threshold velocity), shifting the ratio $A_2/2A_1$. Recognizing that a smaller
428　threshold velocity is associated with smaller grain size, the comparison between Figure 12a and
429　12b suggests that patch-interaction has a weaker impact on finer suspended loads.
430　　　　To illustrate the different feedbacks observed for the upstream and downstream patches,
431　Figure 13 shows the dependence on L/D and T/D of the nondimensional upstream deposition
432　area, A_u/A_1, and the nondimensional downstream deposition area, A_d/A_1 for the $u/U_0 < 0.5$
433　threshold. We can only discuss the lower threshold velocity, because for $u/U_0 < 0.7$, the
434　secondary deposition zones often merged with the primary deposition zones, making it
435　impossible to define A_u and A_d separately for all T/D and L/D arrangements. We particularly
436　focus on the feedbacks for staggered patch configurations ($L/D \geq 1$). Due to the biased flow
437　described in section 3.4, the deposition zone of the upstream patch was always diminished,
438　relative to an isolated patch, with the greatest reduction ($A_u/A_1 = 0.24$) occurring at $L/D = 1$, T/D
439　$= 1$ (Fig. 13a). As the longitudinal spacing (L) increased, this negative feedback gradual
440　declined and disappeared for $L/D > \approx 8$, i.e. $A_u/A_1 = 1.0 \pm 0.1$ for $L/D > 8$. The deposition zone
441　associated with the downstream patch was always enhanced, with maximum enhancement
442　($A_d/A_1 = 2.79$) occurring for $L/D = 1$ and $T/D = 1$. For patches with lateral spacing less than
443　$1.3D$, the enhanced deposition area occurred for all longitudinal spacing considered. Notably,
444　the positive feedback for the downstream patch extended over larger patch spacing than the
445　negative feedback on the upstream patch. For patches with lateral spacing greater than $1.5D$,
446　the feedback was eliminated at longitudinal spacing around $L/D = 8$, similar to the limit of influence
447　on the upstream patch.
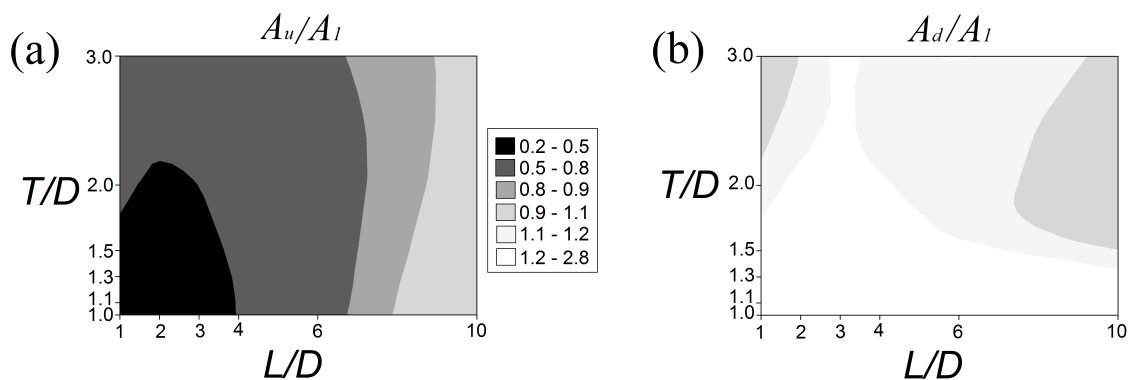
448
449　**Fig. 13** Nondimensional deposition area as a function of L/D and T/D for $u/U_0 < 0.5$: (a) A_u/A_1, nondimensional
450　upstream patch deposition area; (b) A_d/A_1, nondimensional downstream patch deposition area.

451　**3.6　Implications for large-scale landscape evolution**

452   The numerical study of two-patch interactions can provide some insight into large-scale
453   landscape evolution. We specifically compared two scenarios, one for which the initial patch
454   spacing was large enough to produce no patch-to-patch feedback, and one for which the initial
455   patch-to-patch spacing was small enough to produced strong feedbacks. The initial state for the
456   first scenario is shown in Fig. 14a. The longitudinal and transverse spacing between the patches
457   was sufficient ($T/D> 8$, $L/D> 8$) to initially produce, a deposition zone similar to an isolated
458   patch behind each individual patch (Fig. 14b). If the patches grew into these deposition regions,
459   the individual patches lengthen, but do not widen. Meanwhile, due to flow diversion away from
460   the patches, the flow between the patches is elevated, which inhibits patch expansion and
461   maintains these bare regions (e.g. see discussion of the influence of bare regions in [17]). We
462   conjecture that the patches will continue to grow only in the streamwise direction, eventually
463   forming a landscape dominated by flow-parallel regions of vegetation and channel (Fig. 14c).
464   This configuration is likely to be stable, because the high velocities in the bare adjacent areas
465   inhibit expansion of vegetation into these zones. Thus, we conjecture that the vegetation will
466   evolve to a state characterized by relatively stable channels and well-defined vegetated regions
467   (with a width of the order of D) (see Fig. 14c). The end pattern of this scenario is similar to
468   observations from the field and previous numerical simulations. For example, Bernhardt and
469   Willard [24] observed, in the Florida Everglades, a landscape characterized by longitudinally
470   oriented ridges of vegetation and open-water sloughs (see Fig. 3 in [24]). Through process-
471   based numerical modeling, Larsen and Harvey [6] have also reproduced a landscape with
472   parallel preferential flow channels (see the category "Parallel Preferential Flow Channels" in
473   [6], Fig. 1). Fig. 14d presents an actual landscape from the Florida Everglades (26°09'45.6"N
474   80°40'21.9"W), obtained from Google Maps, which closely resembles the final state proposed
475   in Fig. 14c.
476   In the second scenario (Fig. 14e), the patches were initially placed close enough that
477   patch-to-patch feedbacks would occur, specifically the initial patch spacing fell in the parameter
478   space (L, T) for biased flow (Fig. 11) and negative feedbacks to the upstream patch (Fig. 13a).
479   We assumed that the deposition behind each patch would depend only on the position of its
480   nearest neighbor vegetation patch. For example, if patch A was located at $x = 0$ and $y = 0$ and
481   the nearest downstream vegetation patch B was $x = 6D$ and y = $1.5D$, then the deposition area
482   behind patch A was assumed to follow that observed numerically for a pair of patches separated
483   by $L/D = 6$ and $T/D = 1.5$, e.g. as shown in Figure 11d. Letting the vegetation patches in Figure
484   14e grow into their respective deposition areas yields the new landscape shown in Fig. 14f. The
485   accelerate flows between the patches may limit further patch growth, so that the landscape
486   evolves to a mosaic of small patches of different patch length, but generally elongated parallel
487   to the flow. A distribution of patch sizes aligned preferentially to the flow (as shown in Fig. 14f)
488   is consistent with observations of freshwater macrophyte distributions in a lowland river in
489   Belgium [25] and in Scotland [26]. Larsen and Harvey [6] produced a similar landscape pattern
490   within their landscape evolution model (see the category "Small Elongated Islands" in [6], Fig.
491   1). Finally, Figure 14g presents an actual landscape from Florida Everglades (26°01'35.2"N
492   80°50'19.1"W), obtained from Google Maps, which closely resemble our second scenario.
493   The two scenarios consider here highlight the potential role of initial patch spacing on
494   landscape patterns. If pioneer vegetation is sparsely distributed (patch spacing larger than $10D$),
495   the feedback to deposition and additional plant growth may tend toward a channeled landscape
496   (Fig. 14d). If the pioneer vegetation is densely distributed (patch spacing less than $6D$, based on
497   Fig. 13), patch interaction tends to shorten the deposition zones, limiting patch expansion,
498   resulting in a mosaic of patch sizes generally elongated in the streamwise direction (Fig. 14f).
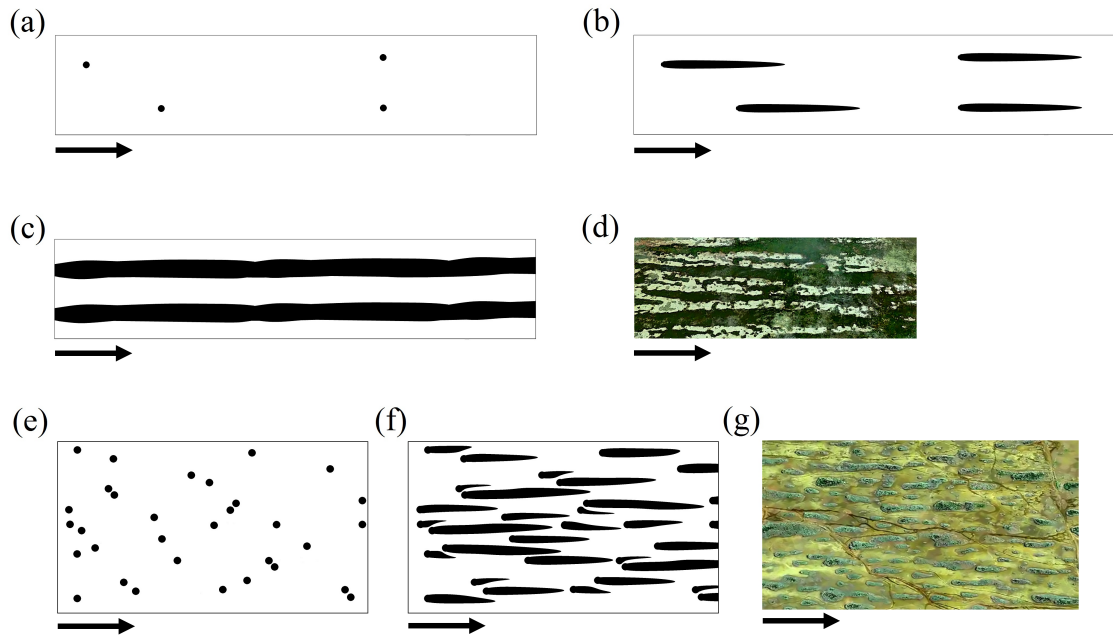
Fig. 14 (a)-(c). Evolution of a vegetated landscape starting from sparsely distributed pioneer vegetation. (a) Initial longitudinal and transverse spacing between the patches is sufficient to produce no patch-to-patch interaction. (b) Deposition area added behind each patch is the same as that behind an isolated patch (c) Conjectured final landscape characterized by relatively stable channels (bare regions) and well-defined vegetated regions. (d) A landscape (26°09'45.6"N 80°40'21.9"W), obtained from Google Maps, which closely resembles conjectured landscape in (c). (e)-(f). Evolution of a vegetated landscape starting from (e) closely distributed pioneer vegetation. The initial spacing is small enough ($L/D < 6$) to limit the wake growth and deposition areas of each patch, yielding a distribution of small patches as a final state (f) characterized by elongated vegetation patches oriented parallel to the flow. (g) An actual landscape (26°01'35.2"N 80°50'19.1"W), obtained from Google Maps, which closely resemble (f).

4 Conclusions

This study examined the flow field and inferred deposition patterns around two nearby circular patches of vegetation using Computational Fluid Dynamics (CFD). The following trends were observed for the threshold velocity $u/U_o < 0.5$. When the two patches were far from each other ($L/D > 8$, $T/D > 8$), wake interaction was weak and flow and deposition patterns around each patch resembled those of a single, isolated patch. When the two patches were close enough ($L/D < 8$, $T/D < 8$), both positive and negative feedbacks to wake scale and inferred deposition area were observed. For side-by-side patches ($L/D = 0$), the total deposition area was enhanced (positive feedback) for small gaps ($L/D < 1.5$) but diminished (negative feedback) for large gaps ($T/D > 1.5$, based on Fig. 12a). For staggered patches ($L/D \geq 1$), the flow between the patches deflected lateral toward the upstream patch, which shortened the upstream patch wake and diminished its deposition area, relative to an isolated patch (negative feedback). The downstream patch in a staggered pair exhibited a positive feedback, with the wake length and deposition area both enhanced, relative to an isolated patch. The interaction between staggered patches may explain the landscape consisting of a distribution of small patch sizes generally aligned with the flow (Fig. 14g) which is often observed in rivers.

532

References

534 1. Kemp, J. L., Harper, D. M., Crosa, G.A., 2000. The habitat-scale ecohydraulics of rivers,
535 Ecological Engineering. 16 (1), 17-29, doi: 10.1016/S0925-8574(00)00073-2.

536 2. Wilcock, R., Champion, P., Nagels, J. Crocker, G., 1999. The influence of aquatic
537 macrophytes on the hydraulic and physico-chemical properties of a New Zealand lowland
538 stream, Hydrobiologia, 416, 203-214, doi:10.1023/A:1003837231848.

539 3. Jones, J.I., Collins, A.L., Naden, P.S., Sear, D.A., 2012. The relationship between fine
540 sediment and macrophytes in rivers. River Research and Applications 28: 1006–1018.

541 4. Pollen-Bankhead, N., Simon, A., 2010. Hydrologic and hydraulic effects of riparian root
542 networks on streambank stability: Is mechanical root-reinforcement the whole story?
543 Geomorphology 116 (3-4), 353-362.

544 5. Van De Wiel, M., Couthard, T., Macklin, M., Lewin, J., 2007. Embedding reach-scale fluvial
545 dynamics within the CAESAR cellular automaton landscape evolution model. Geomorphology
546 90, 283-301.

547 6. Larsen, L.G., Harvey, J.W., 2011. Modeling of hydroecological feedbacks predicts distinct
548 classes of landscape pattern, process, and restoration potential in shallow aquatic ecosystems.
549 Geomorphology 126, 279–296.

550 7. Vandenbruwaene, W., Temmerman, S., Bouma, T., Klaassen, P., de Vries, M., Callaghan, D.,
551 van Steeg, P., Dekker, F., van Duren, L. A., Martini, E., Balke, T., Biermans, G., Schoelynck,
552 J., Meire, P. (2011). Flow interaction with dynamic vegetation patches: Implications for
553 biogeomorphic evolution of a tidal landscape. Journal of Geophysical Research-Earth Surface
554 116.

555 8. Bennett, S., Wu, W., Alonso, C.V., Wang, S.Y., 2008. Modeling fluvial response to instream
556 woody vegetation: implications for stream corridor restoration. Earth Surface Processes and
557 Landforms 33, 890–909.

558 9. Follett, E.M., Nepf, H.M., 2012. Sediment patterns near a model patch of reedy emergent
559 vegetation. Geomorphology 179, 141–151.

560 10. Neary, V.S., Constantinescu, S.G., Bennett, S.J., Diplas, P., 2012. Effects of Vegetation on
561 Turbulence, Sediment Transport, and Stream Morphology. Journal of Hydraulic Engineering
562 138, 765–776.

563 11. Rominger, J.T., Nepf, H.M., 2011. Flow adjustment and interior flow associated with a
564 rectangular porous obstruction. Journal of Fluid Mechanics 680, 636–659.

565 12. Zong, L., Nepf, H.M., 2011. Spatial distribution of deposition within a patch of vegetation.
566 Water Resources Research 47, doi: 10.1029/2010WR009516.

567   13. Bouma, T.J., van Duren, L.A., Temmerman, S., Claverie, T., Blanco-Garcia, A., Ysebaert,
568   T., Herman, P.M.J., 2007. Spatial flow and sedimentation patterns within patches of epibenthic
569   structures: combining field, flume and modelling experiments. Continental Shelf Research 27
570   (8), 1020–1045.

571   14. Rominger, J.T., Lightbody, A.F., Nepf, H.M., 2010. Effects of added vegetation on sand bar
572   stability and stream hydrodynamics. Journal of Hydraulic Engineering 136 (12), 994–1002.

573   15. Tsujimoto, T., 1999. Fluvial processes in streams with vegetation. Journal of Hydraulic
574   Research 37 (6), 789–803.

575   16. Chen, Z., Ortiz, A., Zong, L., Nepf, H., 2012. The wake structure behind a porous
576   obstruction and its implications for deposition near a finite patch of emergent vegetation. Water
577   Resourcers Research 48.

578   17. Meire, D., Kondziolka, J., Nepf, H., 2014. Interaction between neighboring vegetation
579   patches: Impact on flow and deposition. Water Resourcers Research 50 (5):3809-3825, doi:
580   10.1002/2013WR015070

581   18. Zong, L., Nepf, H., 2012. Vortex Development behind a finite porous obstruction in a
582   channel. Journal of Fluid Mechanics, 691, 368-391, doi:10.1017/jfm.2011.479.

583   19. Fluent Inc, User's Guide, release 14.5.7, 2014.

584   20. Stoesser, T., Kim, S. J., Diplas, P., 2010. Turbulent flow through idealized emergent
585   vegetation. Journal of Hydraulic Engineering 136, 1003-1017.

586   21. Tian, X., Ong, M., Yang, J., Myrhaug, D., 2013. Unsteady RANS simulations of flow
587   around rectangular cylinders with different aspect ratios. Ocean Engineering 58, 208–216.

588   22. Sand-Jensen, K., 1998. Influence of submerged macrophytes on sediment composition and
589   near-bed flow in lowland streams. Freshwater Biology 39 (4):663–679.

590   23. Christiansen, E.H. et al. Dynamic Earth. Jones & Bartlett Publishers, 2014. Print.

591   24. Bernhardt, C.E., Willard, D.A., 2009. Response of the Everglades' ridge and slough
592   landscape to late Holocene climate variability and 20th century water-management practices.
593   Ecological Applications 19, 1723–1738.

594   25. Schoelynck, J., De Groote, T., Bal, K., Vandenbruwaene, W., Meire, P., Temmerman, S.,
595   2012. Self-organized patchiness and scale-dependent bio-geomorphic feedbacks in aquatic river
596   vegetation. Ecography 35, 760–768.

597   26. Cameron, S. M., Nikora, V. I., Albayrak, I., Miler, O., Stewart, M., Sniscalchi, F., 2013.
598   Interactions between aquatic plants and turbulent flow: a field study using stereoscopic PIV.
599   Journal of Fluid Mechanics 732, 345–372.